Supplementary Information to:

Effect of Crystal Packing on the Excitonic Properties of Rubrene Polymorphs

Xiaopeng Wang,[a] Taylor Garcia,[b] Stephen Monaco,[b] Bohdan Schatschneider[b,c] and Noa Marom*[a]

a. Department of Materials Science and Engineering, Carnegie Mellon University, Pittsburgh, Pennsylvania 15213, USA
b. Department of Chemistry, The Pennsylvania State University, Fayette- The Eberly Campus, Uniontown, Pennsylvania 15401, USA
c. Chemistry and Biochemistry Department, California State Polytechnic University at Pomona, Pomona, California 91768, USA
* Email: nmarom@andrew.cmu.edu

I. Temperature dependence of the relative stability of the three rubrene polymorphs
II. Pressure dependence of triclinic rubrene
III. Effect of pressure on the electronic properties of the rubrene polymorphs
IV. GW results for a rubrene molecule
V. Convergence of the GW and BSE calculations for crystalline rubrene
VI. G_0W_0+BSE@PBE results for crystalline pentacene
VII. References

I. Temperature dependence of the relative stability of the three rubrene polymorphs
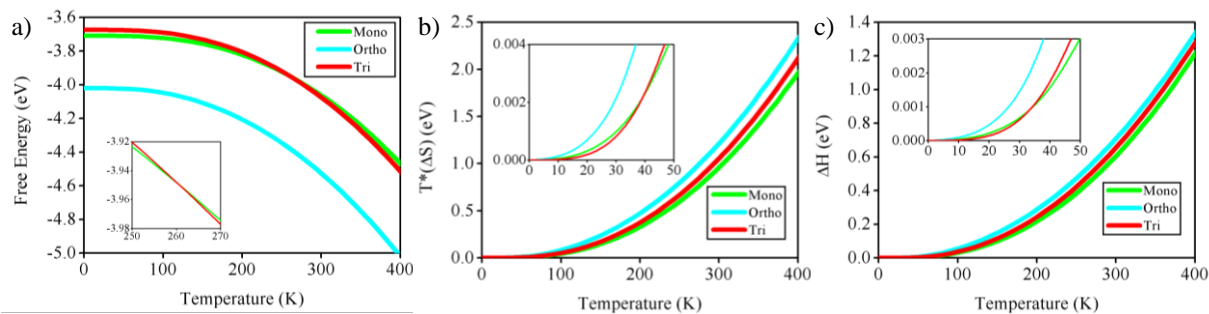

Fig. S1 Thermodynamic properties of rubrene polymorphs: (a) free energy, (b) the entropic contribution to the free energy, and (c) the enthalpy (cohesive energy). The initial value for ΔG is ΔH$_{lattice}$. All quantities are reported per molecular unit.

The calculated temperature dependence of the thermodynamic properties of the three rubrene polymorphs is shown in Fig. S1. It can be seen from Fig. S1a that the free energy of the orthorhombic structure is the lowest of the three polymorphs over a wide temperature range, indicating that it is the most stable of the three. The monoclinic and triclinic forms are close in energy to each other with a phase transition occurring at about 263 K. If the free energy of the molecule in any phase is assumed to be the same, the variation in the crystalline free energies of each polymorph is the result of variations in the packing and corresponding intermolecular interactions. The reason for the enhanced stability of the orthorhombic form is that it possesses the largest amount of entropy of the three polymorphs as shown in Fig. S1b. The high entropy of the orthorhombic structure may be linked with the highest number of closer than vdW contacts of the three polymorphs as evaluated via Hirshfeld surface analysis.[1] The enthalpy (cohesive energy) of the three polymorphs is shown in Fig. S1c. Here, the orthorhombic phase has the largest value. It has been shown in other large-scale studies of gas phase polyaromatic hydrocarbons (PAHs) that the larger the

cohesive energy of a PAH within a given family, the smaller the band gap.[2] This is consistent with our findings regarding the different polymorphs of rubrene; i.e., the orthorhombic phase has the smallest band gap and the largest relative enthalpy, whereas the monoclinic phase has the smallest enthalpy and the largest band gap.

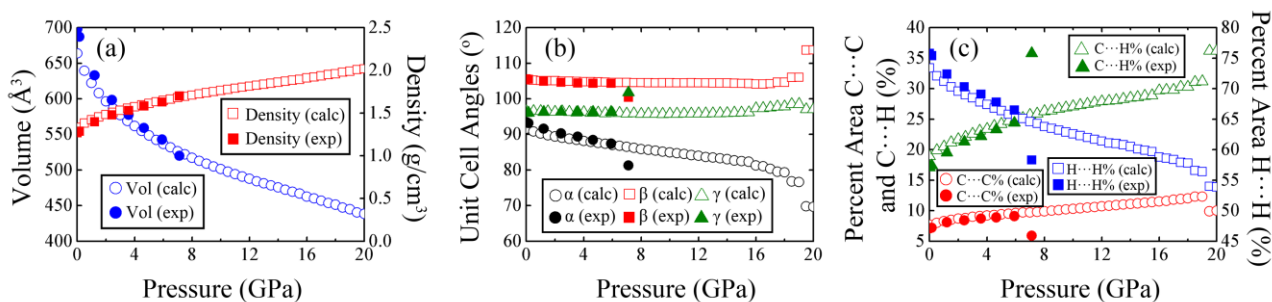## II. Pressure dependence of triclinic rubrene

Fig. S2 Pressure response of triclinic rubrene, compared to experimental data from Ref. 3: (a) volume per molecule and density, (b) unit cell angles, and (c) Hirshfeld surface pressure dependence.

Comparison of the pressure dependent changes in the triclinic structure from PBE+TS and experiment[3] is shown in Fig. S2. It has been observed experimentally that above 6 GPa that the triclinic phase (form I) adopts a previously undefined morphology (form II). This transformation is demonstrated via discontinuities in the pressure dependence of the unit cell parameters and intermolecular close contacts. Excellent agreement is achieved between experiment and PBE+vdW until the phase transition to form II occurs above 6 GPa. However, the experimentally observed discontinuities are captured in the simulations at higher pressures. Discontinuities in the pressure dependence of the calculated unit cell parameters seen in Fig. 2 in the main text and Fig. S2a demonstrate a transition similar to that observed experimentally from form I to form II. The onset of the calculated transition starts at ~16 GPa with the expansion of the c unit cell axis and the compression of b unit cell axis. While the unit cell axes have small fluctuations starting at ~16 GPa, they do not display the large discontinuity observed experimentally until ~19 GPa.

It can be seen in Fig S2c that the percent H···H contacts decrease with pressure while the percent C···H and C···C contacts increase until the calculate phase transition pressure of 19 GPa. This is similar to the increase in packing efficiency in response to stress, observed for other PAHs[4] and heterocycles.[5] It is interesting to note that the H···H and C···H contacts change at similar but opposite rates (~1% per GPa) while the C···C contacts change at a quarter that rate (~0.25% per GPa). Discontinuities are observed in the pressure dependence of the close contact fractions at the same pressure as observed for the unit cell parameters. Here, both the C···C and H···H contacts decrease while the H···H contacts increase, in agreement with the experimentally observed pressure dependent phase transition.

The simulated high pressure structures are presented in Fig S3. It is evident that the tetracene backbone becomes increasingly twisted with increasing pressure and that the lateral phenyl rings begin to scissor and twist from 90 degrees with the tetracene backbone, in agreement with experiment. We also see the "opening angle" and "torsion angle" of the lateral phenyl rings decrease as observed experimentally (see SI of Ref. 3 for angle definitions).
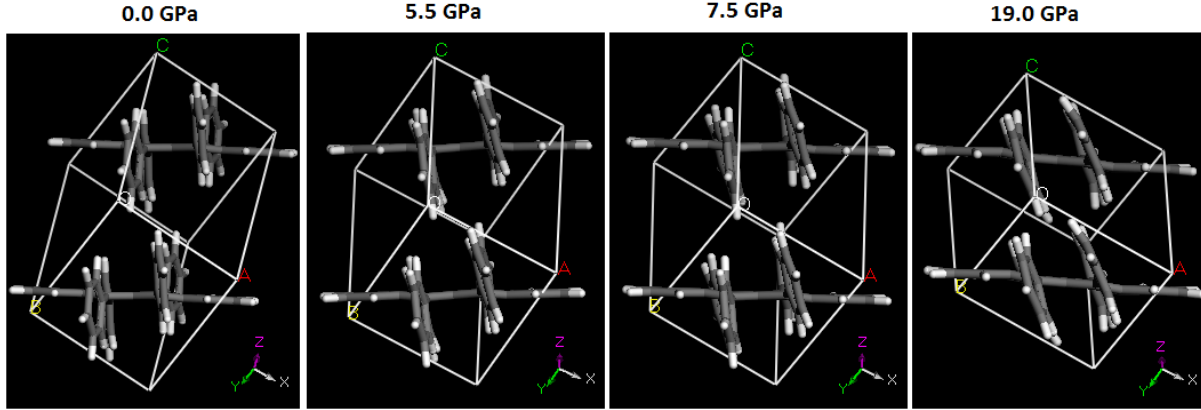
| 0.0 GPa | 5.5 GPa | 7.5 GPa | 19.0 GPa |

Fig. S3 Geometry optimized triclinic rubrene structures at different pressures.

III. Effect of pressure on the electronic properties of the rubrene polymorphs

The electronic and excitonic properties of molecular crystals often exhibit a strong pressure response, owing to the nature of weak dispersive intermolecular interactions, which facilitates structural and conformational changes.[3-9] Here, we use PBE for a qualitative analysis of the effect of pressure on the electronic properties of the rubrene polymorphs. Structural relaxation under pressure was performed with PBE+TS using the CASTEP code as detailed in the main text. Single point calculations for the relaxed structures were performed with the FHI-aims code,[10, 11] using tight numerical settings and tier 2 basis sets. The change in the band gap is estimated based on PBE calculations and referenced to the G_0W_0@LDA gap at zero pressure. Similarly, the change in the top valence band and bottom conduction band is obtained from PBE band structures and referenced to zero pressure G_0W_0@LDA values. The change in the triplet excitation energy is calculated based on the PBE total energy differences between the singlet ground state and the triplet spin configuration.

Fig. S4 shows the estimated pressure dependence of the band gaps, the band dispersion, and the triplet excitation energies of the three forms. The band gaps of all three polymorphs decrease, similar to other PAHs.[4] This is consistent with the experimentally observed typical red shift of the absorption spectra of organic semiconductors under pressure.[12] For all three polymorphs, the band dispersion increases with pressure. This is consistent with the experimentally observed enhancement in the mobility of orthorhombic rubrene under pressure.[6, 8] For the monoclinic form the triplet excitation energy decreases with pressure at a similar rate to the PBE gap, which we assume to correlate with the rate of decrease of the singlet excitation energy. Therefore, at least in terms of the energy conservation requirement we do not expect a significant change in SF efficiency. The increase in band dispersion may make the singlet
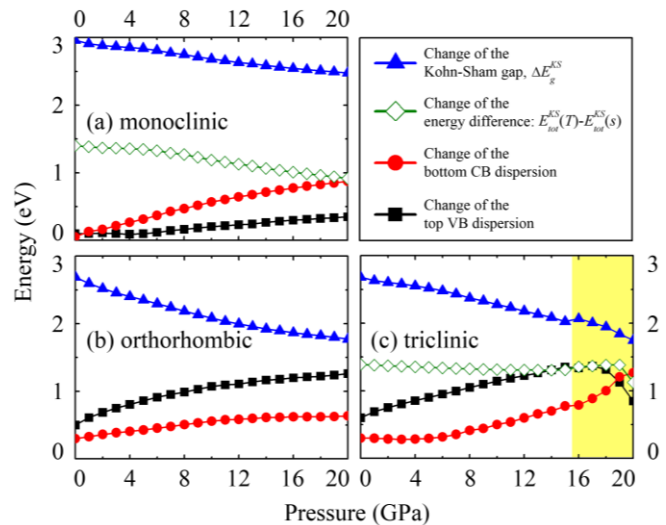

Fig. S4 pressure dependence of the electronic properties of (a) monoclinic, (b) orthorhombic, and (c) triclinic rubrene, estimated based on PBE calculations. Energies at 0 GPa in this figure are referenced to the *GW* values listed in Table 2 in the main text. The yellow region in (c) represents the phase transition of the triclinic form.

exciton more FK-like, which may reduce SF efficiency. For the triclinic form, we estimate that while the triplet excitation energy remains almost constant with the increase in pressure, the singlet excitation energy decreases significantly. Therefore, the effect of pressure is detrimental to SF efficiency. This is consistent with the observation of decreased SF rate in tetracene under pressure.[13]

The rate of gap decrease for each polymorph varies over different pressure ranges. The monoclinic phase has the smallest band gap pressure dependence. This is due in part to the fact that the tetracene backbones do not overlap well in this polymorph (see Fig. 5 in the main text). Therefore, the pressure increase results in a minimal increase in the intermolecular overlap of the frontier orbitals. Since the frontier orbitals are primarily concentrated on the carbon atoms of the tetracene backbone, one can monitor the increased interaction between the frontier orbitals of neighbouring molecules by calculating the pressure dependence of the C···C intermolecular interactions via Hirshfeld surface analysis. Fig. S5 demonstrates that the rate of increase in %C···C intermolecular interactions as

Fig. S5 Comparison of intermolecular close contacts, derived from Hirshfeld surface analysis, as a function of pressure for the monoclinic, orthorhombic, and triclinic phases of rubrene.

a function of pressure is smallest for the monoclinic phase (monoclinic 0.126 %C···C/GPa, orthorhombic 0.154 %C···C/GPa, triclinic 0.179 %C···C/GPa). In addition, it has been shown that the %C···C interaction on the Hirshfeld surface is directly correlated with the band gap in PAHs,[14] and the monoclinic phase starts with nearly no C···C intermolecular interactions under ambient conditions.[1] As a result of the initially poor overlap of the frontier orbitals and/or the low %C···C contacts, the band gap pressure response is half that of the other phases. Another factor contributing to the decreased band gap pressure response of the monoclinic phase is that while the dispersion of the bottom conduction band increases immediate upon pressurization, the top valence band remains essentially unchanged up to about 5 GPa. As seen from the other phases, the dispersion of the top valence band seems to have the most significant effect on closing the band gap.

Greater overlap of the frontier orbitals is present in the orthorhombic and triclinic polymorphs at 0 GPa (see Fig 5 in the main text), causing a more sensitive pressure dependence of the band gaps. This increased overlap of the frontier orbitals can also be captured via the %C···C intermolecular interactions at 0 GPa in Fig. S3. It is observed in Figures S4 and S5 that while the triclinic phase has the greatest rate of increase in the %C···C intermolecular interactions, the orthorhombic phase has the greatest decrease in the PBE gap. This is because the triclinic phase undergoes a polymorphic phase transition over the pressure range of interest, causing an upward discontinuity in the downward progression of the band gap pressure dependence.

When the band gap pressure dependence of each polymorph is compared with that of pentacene, it is observed that the lateral phenyl rings of rubrene work effectively as cushions between the localized frontier orbitals on backbones to decrease the pressure effect. Therefore the collapse in the band gap for rubrene in all morphologies (-0.024 eV/GPa for monoclinic, -0.045 eV/GPa for orthorhombic, and -0.044 eV/GPa for triclinic forms) is at most half of that observed for pentacene (-0.08 eV/GPa)[4, 9] over the same pressure range. This can be explained in part by the fact that the %C···C intermolecular interactions occurring on the Hirshfeld surface of pentacene increase at quadruple the rate of any rubrene polymorph over the same pressure region.[4]
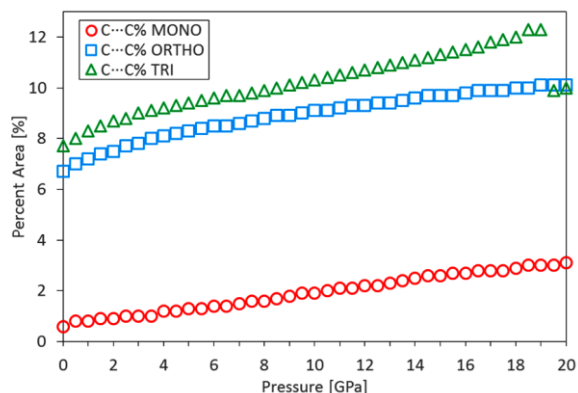
IV. *GW* results for a rubrene molecule

Table S1 The IP, EA, and fundamental gap in eV of a single rubrene molecule in geometries corresponding to the monoclinic, orthorhombic, and triclinic polymorphs obtained with G_0W_0 based on different mean-field starting points.

	Molecule @ Monoclinic			Molecule @ Orthorhombic			Molecule @ Triclinic		
	G_0W_0 @HF	G_0W_0 @PBE	G_0W_0 @PBE0	G_0W_0 @HF	G_0W_0 @PBE	G_0W_0 @PBE0	G_0W_0 @HF	G_0W_0 @PBE	G_0W_0 @PBE0
IP	6.78	6.14	6.32	6.79	6.14	6.32	6.80	6.15	6.34
EA	1.28	1.82	1.62	1.31	1.83	1.63	1.28	1.81	1.61
Gap	5.50	4.32	4.70	5.48	4.31	4.69	5.52	4.34	4.72

G_0W_0 calculations for a rubrene molecule were performed with the FHI-aims code,[10, 11, 15] using *tier 4* basis sets. For the mean-field starting point we used the generalized gradient approximation of Perdew, Burke, and Ernzerhof (PBE),[16, 17] the PBE-based hybrid functional (PBE0)[18] with 25% Fock exchange, and Hartree-Fock. The geometry of the rubrene molecule in the three polymorphs varies slightly because the different crystal packing leads to small changes in the orientation of the phenyl side groups. Our G_0W_0 calculations show that the electronic properties of a single rubrene molecule are not sensitive to this slight difference in geometry. As shown in Table S1, the energy differences in the ionization potential (IP), electron affinity (EA) and fundamental gap (IP-EA) are within 0.03 eV. The calculated valence spectra are compared to a gas phase photoemission spectroscopy (PES) experiment[19] in Fig. S6. The
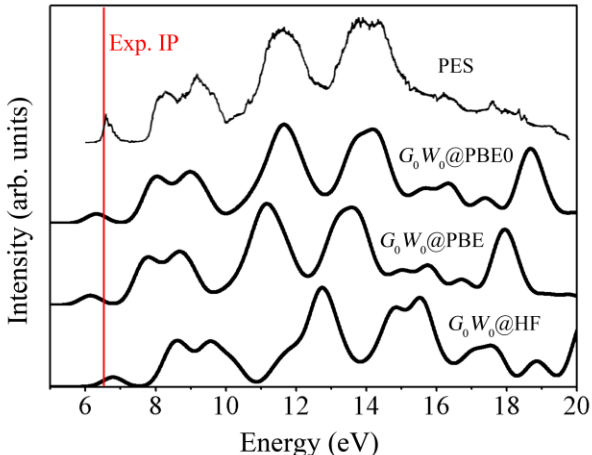

Fig. S6 Spectra of a rubrene molecule obtained with G_0W_0 calculations based on different mean-field starting points, broadened by a 0.3 eV Gaussian, compared to PES data from Ref. 19. The red line represents experimental IP.

best agreement with experiment is obtained with G_0W_0@PBE0, while the G_0W_0@PBE and G_0W_0@HF spectra are shifted to lower and higher ionization energies, respectively. The good performance of the PBE0 starting point for valence spectra is consistent with the results of earlier studies for other organic semiconductors.[20-24] We note that the results of G_0W_0 calculations may vary somewhat between different implementations.[25] It has been shown that the G_0W_0@PBE results of the BerkeleyGW code are similar to the G_0W_0@PBE0 results of FHI-aims.[26] This may be attributed to favorable error cancellation between the gap underestimation by PBE and the gap overestimation resulting from the Hybertsen-Louie generalized plasmon pole model.[27-29] Here, we use of the BerkeleyGW code to perform G_0W_0@LDA calculations for molecular crystals of rubrene.

V. Convergence of the *GW* and BSE calculations for crystalline rubrene

G_0W_0 results are known to be sensitive to the convergence of the basis sets, k-point sampling, and other parameters of the calculation.[30-32] Here, the convergence of the G_0W_0@LDA band gap was carefully examined for triclinic rubrene, whose smaller unit cell size allows for performing very tightly converged calculations. The results are shown in Fig. S5. In addition to the k-point sampling (Fig. S7a) and plane-wave cutoff (Fig. S7b) used for the underlying DFT calculation, three parameters must be converged in the *GW* step: the number of bands in the Coulomb hole summation (Fig. S7c), the screened Coulomb cutoff (Fig S7d), and the number of bands in the calculation of the dielectric function (fig. S7e). When testing one parameter, the other two were set to a very large value, which was regarded as 'infinite' value.

The parameter being tested was decreased from 'infinite' value to lower values. Convergence was assessed at four different k points in terms of the difference from the gap obtained with "infinite" tightly converged values. The "infinite" values adopted here for the three *GW* parameters were 5000 bands in the Coulomb hole summation, 50 Ry for the screened Coulomb cutoff, and 5000 bands in the calculation of the dielectric function. The results show that the gaps obtained with values of 600 bands, 20 Ry, and 600 bands, respectively are adequately converged. With these well converged values we further tested the parameters of the LDA calculations. A 2×2×2 k-point grid and a 60 plane-wave cutoff are found to be well converged. The total gap error with our chosen parameter values is about 60 meV.

The k-point convergence of the BSE calculation was tested for the orthorhombic form of rubrene, for which experimental data are available. 12 valence bands and 15 conduction bands were used for the calculation while the k-point grid was varied. The results are shown in Fig. S8. The position of the first absorption peak, which corresponds
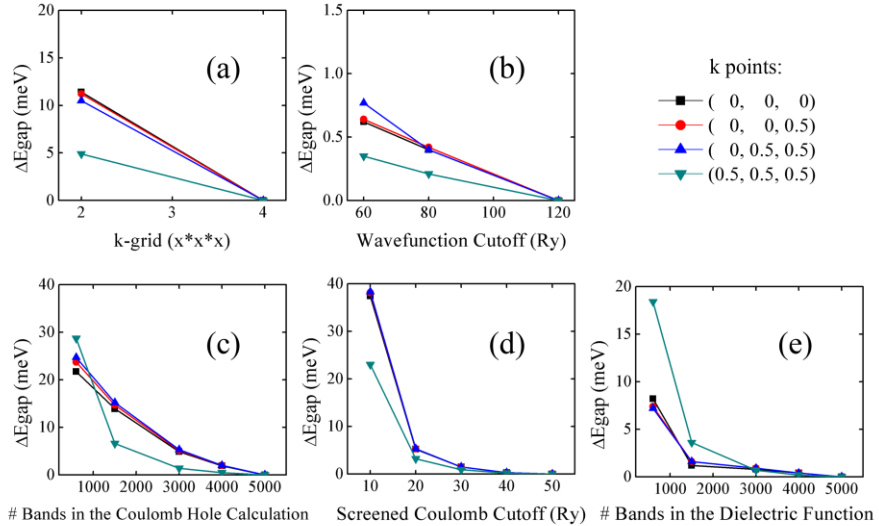

Fig. S7 Convergence of the G_0W_0@LDA band gaps at different k points for triclinic rubrene with respect to (a) k-point sampling, (b) the plane-wave cutoff, (c) the number of bands in the Coulomb hole calculation, (d) the screened Coulomb cutoff, and (e) the number of bands in the dielectric function calculation. The error in the gap is given in meV with respect to the tightly converged "infinite" value.
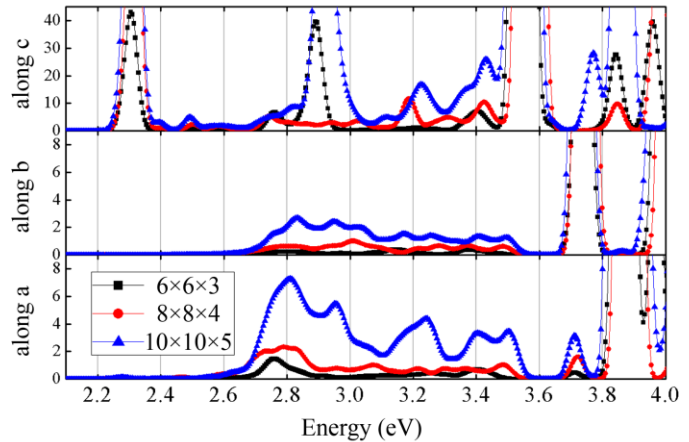

Fig. S8 G_0W_0+BSE@LDA absorption spectra for light polarized along the three crystal axes of orthorhombic rubrene, calculated with different k-point grids.

to the singlet excitation energy, is already converged with a 6×6×3 k-point grid. The oscillator strength is more sensitive to the k-point sampling, particularly in the 2.7-3.5 eV region of the spectrum. A peak at about 2.9 eV along the c direction is missing when a k-grid of 8×8×4 is used. Detailed benchmark studies, which are beyond the scope of the present work, are needed to fully understand the origin of this behavior. The results reported in the main paper were obtained with a 10×10×5 k-grid, which is the limit of what is computationally feasible presently to the large system size (280 atoms).

G_0W_0+BSE@PBE results for crystalline pentacene

In the following we provide the results of G_0W_0+BSE@PBE calculations for crystalline pentacene, in support of the comparison between rubrene and pentacene in Table 2 of the main text. These calculations were conducted as a part of a different project and will be published independently elsewhere. We note that the results of G_0W_0 based on PBE and LDA have been shown to be very similar (see the SI of Ref. 22 and Table S2). The PBE eigenvalues and wave-functions were generated with Quantum Espresso,[33] using a k-point grid of 4×4×2 and plane-wave energy cutoff of 50 Ry. G_0W_0+BSE calculations were performed with the BerkeleyGW code.[31] 568 bands and a screened Coulomb cutoff of 10 Ry were used for the G_0W_0 calculation. 24 valence bands, 24 conduction bands and a k-grid of 8×8×4 were used for the BSE calculation. Fig. S9 shows the G_0W_0@PBE band structure, which is in agreement with Ref. 34. A comparison of the fundamental gap is also provided in Table S2. The k-point convergence of the BSE calculation is shown in Fig. S10 for absorption spectra summed over all polarizations. The absorption spectra obtained with k-point grids of 8×8×4 and 4×4×2 have the same form. Denser k-point sampling leads to a shift of the spectrum to higher energies by about 0.1 eV. Our results are in agreement with Ref. 35, as shown in Table S2.
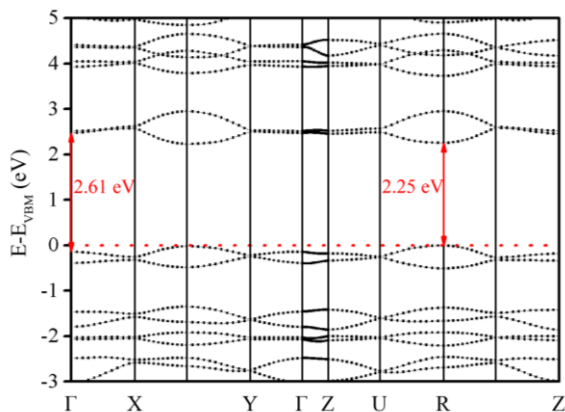

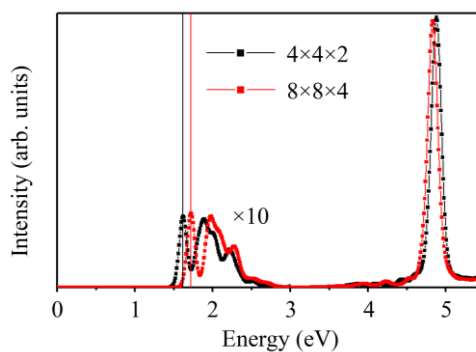**Fig. S9** G_0W_0@PBE band structure of crystalline pentacene.

Fig. S10 G_0W_0+BSE@PBE absorption spectra of crystalline pentacene calculated with a k-point grid of 4×4×2 (black) and 8×8×4 (red). Vertical lines represent optical gaps. The spectra are scaled for ease of comparison and the region under 3 eV is multiplied by 10 for clarity.

Table S2 Fundamental and optical gaps of crystalline pentacene computed with G_0W_0+BSE@PBE

	k-grid in G_0W_0	Fundamental gap	k-grid in BSE	Optical gap
This work (G_0W_0+BSE@PBE)	4×4×2	2.25 eV	8×8×4	1.72 eV
	4×4×2		4×4×2	1.62 eV
Ref. 35 (G_0W_0+BSE@LDA)	4×4×2	2.1 eV	4×4×2	1.64 eV

VI.   References

1. S. Bergantin and M. Moret, *Crystal Growth & Design*, 2012, **12**, 6035-6041.
2. A. Kuc, T. Heine and G. Seifert, *Phys. Rev. B*, 2010, **81**, 085430.
3. S. Bergantin, M. Moret, G. Buth and F. P. A. Fabbiani, *The Journal of Physical Chemistry C*, 2014, **118**, 13476-13483.
4. B. Schatschneider, S. Monaco, A. Tkatchenko and J.-J. Liang, *The Journal of Physical Chemistry A*, 2013, **117**, 8323-8331.
5. B. Schatschneider and J. J. Liang, *The Journal of Chemical Physics*, 2011, **135**, 164508.
6. Y. Okada, K. Sakai, T. Uemura, Y. Nakazawa and J. Takeya, *Phys. Rev. B*, 2011, **84**, 245308.

7. K. Sakai, Y. Okada, S. Kitaoka, J. Tsurumi, Y. Ohishi, A. Fujiwara, K. Takimiya and J. Takeya, *Phys. Rev. Lett.*, 2013, **110**, 096603.
8. J. Takeya, T. Uemura, K. Sakai and Y. Okada, *Thin Solid Films*, 2014, **554**, 19-26.
9. L. Farina, K. Syassen, A. Brillante, R. G. Della Valle, E. Venuti and N. Karl, *High Pressure Research*, 2003, **23**, 349.
10. V. Blum, R. Gehrke, F. Hanke, P. Havu, V. Havu, X. Ren, K. Reuter and M. Scheffler, *Computer Physics Communications*, 2009, **180**, 2175-2196.
11. V. Havu, V. Blum, P. Havu and M. Scheffler, *Journal of Computational Physics*, 2009, **228**, 8367-8379.
12. M. B. Smith and J. Michl, *Chem. Rev.*, 2010, **110**, 6891-6936.
13. W. B. Whitten and S. Arnold, *physica status solidi (b)*, 1976, **74**, 401-407.
14. B. Schatschneider, S. Monaco, J.-J. Liang and A. Tkatchenko, *The Journal of Physical Chemistry C*, 2014, **118**, 19964-19974.
15. X. Ren, A. Sanfilipo, P. Rinke, J. Wieferink, A. Tkatchenko, K. Reuter, V. Blum and M. Scheffler, *New Journal of Physics*, 2012, **14**, 053020.
16. J. P. Perdew, K. Burke and M. Ernzerhof, *Phys. Rev. Lett.*, 1996, **77**, 3865-3868.
17. J. P. Perdew, K. Burke and M. Ernzerhof, *Phys. Rev. Lett.*, 1997, **78**, 1396-1396.
18. C. Adamo and V. Barone, *J Chem Phys*, 1999, **110**, 6158-6170.
19. T. Takahashi, Y. Harada, N. Sato, K. Seki, H. Inokuchi and S. Fujisawa, *Bull. Chem. Soc. Jpn.*, 1979, **52**, 380-382.
20. N. Marom, X. G. Ren, J. E. Moussa, J. R. Chelikowsky and L. Kronik, *Phys. Rev. B*, 2011, **84**, 195143.
21. T. Körzdörfer and N. Marom, *Phys. Rev. B*, 2012, **86**, 041110(R)
22. N. Marom, F. Caruso, X. Ren, O. T. Hofmann, T. Körzdörfer, J. R. Chelikowsky, A. Rubio, M. Scheffler and P. Rinke, *Phys. Rev. B*, 2012, **86**, 245127.
23. E. Salomon, P. Amsalem, N. Marom, M. Vondracek, L. Kronik, N. Koch and T. Angot, *Phys. Rev. B*, 2013, **87**, 075407.
24. J. W. Knight, X. Wang, L. Gallandi, O. Dolgounitcheva, X. Ren, J. V. Ortiz, P. Rinke, T. Körzdörfer and N. Marom, *J. Chem. Theory Comput.*, 2016, **12**, 615-626.
25. M. J. van Setten, F. Caruso, S. Sharifzadeh, X. Ren, M. Scheffler, F. Liu, J. Lischner, L. Lin, J. R. Deslippe, S. G. Louie, C. Yang, F. Weigend, J. B. Neaton, F. Evers and P. Rinke, *J. Chem. Theory Comput.*, 2015.
26. D. A. Egger, S. Weissman, S. Refaely-Abramson, S. Sharifzadeh, M. Dauth, R. Baer, S. Kümmel, J. B. Neaton, E. Zojer and L. Kronik, *J. Chem. Theory Comput.*, 2014, **10**, 1934-1952.
27. W. Kang and M. S. Hybertsen, *Phys. Rev. B*, 2010, **82**, 085203.
28. M. Stankovski, G. Antonius, D. Waroquiers, A. Miglio, H. Dixit, K. Sankaran, M. Giantomassi, X. Gonze, M. Côté and G. M. Rignanese, *Phys. Rev. B*, 2011, **84**, 241201.
29. J. Lischner, S. Sharifzadeh, J. Deslippe, J. B. Neaton and S. G. Louie, *Phys. Rev. B*, 2014, **90**, 115130.
30. S. Sharifzadeh, I. Tamblyn, P. Doak, P. T. Darancet and J. B. Neaton, *Eur. Phys. J. B*, 2012, **85**, 323
31. J. Deslippe, G. Samsonidze, D. A. Strubbe, M. Jain, M. L. Cohen and S. G. Louie, *Computer Physics Communications*, 2012, **183**, 1269-1289.
32. B. C. Shih, Y. Xue, P. H. Zhang, M. L. Cohen and S. G. Louie, *Phys. Rev. Lett.*, 2010, **105**, 146401.
33. P. Giannozzi, S. Baroni, N. Bonini, M. Calandra, R. Car, C. Cavazzoni, D. Ceresoli, G. L. Chiarotti, M. Cococcioni, I. Dabo, A. D. Corso, S. d. Gironcoli, S. Fabris, G. Fratesi, R. Gebauer, U. Gerstmann, C. Gougoussis, A. Kokalj, M. Lazzeri, L. Martin-Samos, N. Marzari, F. Mauri, R. Mazzarello, S. Paolini, A. Pasquarello, L. Paulatto, C. Sbraccia, S. Scandolo, G. Sclauzero, A. P. Seitsonen, A. Smogunov, P. Umari and R. M. Wentzcovitch, *Journal of Physics: Condensed Matter*, 2009, **21**, 395502.
34. S. Sharifzadeh, A. Biller, L. Kronik and J. B. Neaton, *Phys. Rev. B*, 2012, **85**, 125307.

35. S. Refaely-Abramson, M. Jain, S. Sharifzadeh, J. B. Neaton and L. Kronik, *Phys. Rev. B*, 2015, **92**, 081204.